

Cite this: *Chem. Sci.*, 2023, 14, 10446

All publication charges for this article have been paid for by the Royal Society of Chemistry

# Mn(III)-mediated C–P bond activation of diphosphines: toward a highly emissive phosphahelicene cation scaffold and modulated circularly polarized luminescence†

Bo Yang,<sup>a</sup> Suqiong Yan,<sup>a</sup> Chengbo Li,<sup>c</sup> Hui Ma,<sup>a</sup> Fanda Feng,<sup>a</sup> Yuan Zhang<sup>a</sup> and Wei Huang<sup>ib</sup> \*<sup>ab</sup>

Transition metal mediated C–X (X = H, halogen) bond activation provides an impressive protocol for building polyaromatic hydrocarbons (PAHs) in C–C bond coupling and annulation; however, mimicking both the reaction model and Lewis acid mediator simultaneously in a hetero-PAH system for selective C–P bond cleavage faces unsolved challenges. At present, developing the C–P bond activation protocol of the phosphonic backbone using noble-metal complexes is a predominant passway for the construction of phosphine catalysts and P-center redox-dependent photoelectric semiconductors, but non-noble metal triggered methods are still elusive. Herein, we report Mn(III)-mediated C–P bond activation and intramolecular cyclization of diphosphines by a redox-directed radical phosphonium process, generating phosphahelicene cations or phosphoniums with nice regioselectivity and substrate universality under mild conditions. Experiments and theoretical calculations revealed the existence of the unusual radical mechanism and electron-deficient character of novel phosphahelicenes. These rigid quaternary bonding skeletons facilitated versatile fluorescence with good tunability and excellent efficiency. Moreover, the enantiomerically enriched crystals of phosphahelicenes emitted intense circularly polarized luminescence (CPL). Notably, the modulated CPL of racemic phosphahelicenes was induced by chiral transmission in the cholesteric mesophase, showing ultrahigh asymmetry factors of CPL (+0.51, –0.48). Our findings provide a new approach for the design of emissive phosphahelicenes towards chiral emitters and synthesized precursors.

Received 23rd June 2023  
Accepted 11th August 2023

DOI: 10.1039/d3sc03201a

rsc.li/chemical-science

## Introduction

Organic diphosphines, as a brilliant ligand family for the construction of catalysts, drug discoveries, and semiconducting materials, determine the regioselectivity and stereoselectivity in catalytic processes,<sup>1–4</sup> bioactivities,<sup>5,6</sup> and optoelectronic properties<sup>7,8</sup> because of their robust chiral skeleton, chelating capacity, and commercial availability. Economically, developing synthesis protocols for C–P bond activation from available diphosphines is a concise route for expanding ligand libraries and functional materials.<sup>9–14</sup> Nevertheless, the exploitation of

efficient activation and reconstruction between C–P and C–H bonds remains a significant obstruction due to high bonding energy, strong coordinative ability, and intricate selectivity, where noble metal catalysts ([Pd], [Au], and [Rh]) play a critical role.<sup>14–19</sup>

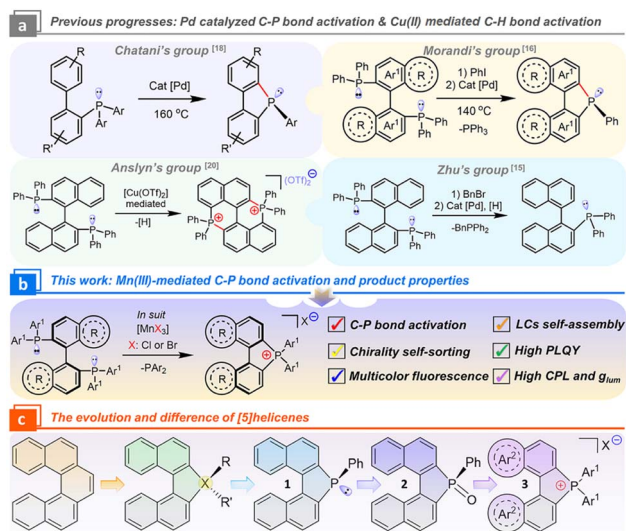
Morandi's group pioneered the C–P bond activation of diphosphines *via* Pd<sub>2</sub>(dba)<sub>3</sub>-catalyzed metathesis (Scheme 1a), and the PPh<sub>3</sub> fragment was eliminated for the cyclopalladated intermediate. Finally, novel neutral phosphahelicenes (P<sup>III</sup>) were generated and further racemic phosphahelicene (P<sup>V</sup>) oxides were isolated.<sup>16</sup> Subsequently, Wang's group modified the reaction to break the intramolecular cyclization of pre-activated phosphoniums.<sup>15</sup> In addition, Cu(OTf)<sub>2</sub>-mediated C–H bond activation at 8,8'-positions in binaphthyl produced an achiral bisphosphonium with a low yield of 24%.<sup>20</sup> This method spread in the laboratory for the preparation of achiral phosphoniums.<sup>21,22</sup> Theoretically, another potential cationic phosphahelicene might be produced after eliminating the PPh<sub>2</sub> unit and rebuilding the C–P bond at the 2'-position. However, this valued phosphahelicene cation ([1b]<sup>+</sup>) and its properties have not been captured and explored (Scheme 3). These above

<sup>a</sup>State Key Laboratory of Coordination Chemistry, School of Chemistry and Chemical Engineering, Nanjing University, Nanjing 210093, P. R. China. E-mail: whuang@nju.edu.cn

<sup>b</sup>Shenzhen Research Institute of Nanjing University, Shenzhen 51805, P. R. China

<sup>c</sup>School of Materials and Energy, University of Electronic Science and Technology of China, Chengdu 610000, P. R. China

† Electronic supplementary information (ESI) available. CCDC 2130476, 2130479, 2130454, 2130459, 2225461, 2225466–2225474, 2225477–2225478, and 2225482. For ESI and crystallographic data in CIF or other electronic format see DOI: <https://doi.org/10.1039/d3sc03201a>



**Scheme 1** (a) Representative C–P bond activation and reconstitution of phosphines. (b) Mn(III)-mediated C–P bond activation and cyclization strategy in this work. (c) Schematic evolution of phosphat[5]helicenes.

described electron-deficient cationic phosphahelicenes that integrated an active C–P bond and a prochiral axis to enhance the oxidative addition efficacy endowed the enantioselective cross-coupling from C–P to C–C bonds with excellent stereoselectivity and regioselectivity.<sup>23</sup> We envisioned that the tunability of metal sources in the pursuit of altering the activation of radical cations and elimination pathways of the intermediates would change the reactivity and selectivity of cyclization.<sup>12,16</sup>

Recently, heterohelicenes have shown arresting renaissance due to their tunable electronic structures, making them widely used in asymmetric catalysis and optoelectronics.<sup>24–28</sup> Notably, the electronic factors are highly dependent on the oxidation state of the phosphorus center in phosphahelicenes. Most neutral phosphahelicenes ( $\text{P}^{\text{III}}$ ) yielded lower quantum efficiency and insufficient CPL because of high nonradiative rates and the fluxional molecular conformation in the excited states (*i.e.*, analogues phosphat[5]helicenes 1 and 2 are not luminescent, Scheme 1c).<sup>29–33</sup> To overcome this drawback, we speculated that introducing a quaternary bonding environment for the P-atom could increase the steric hindrance to reset the electronic transition nature in phosphahelicenes, thereby inhibiting the nonradiative decay of emitters in excited states.<sup>22,34</sup> Furthermore, the cationic phosphahelicene has high stability and electron-defect character in the quaternary C–P bonding environment, providing a new opportunity for the design of chiral donor–acceptor (D–A) modules.<sup>35–37</sup> On the other hand, exploring chiral transmission toward increased CPL of racemic [5]helicenes is still rare.<sup>38,39</sup> Hence, developing highly emissive cationic phosphahelicene scaffolds and chiral self-assembly tactics is an essential extension of heterohelicenes for photoelectric devices and synthesized precursors.

Unprecedentedly, we reported a novel  $\text{MnX}_3$  ( $\text{X} = \text{Cl}, \text{Br}$ ) mediated protocol to construct cationic phosphahelicenes and

phosphoniums from diphosphines (Scheme 1b) *via* intramolecular cyclization with good regioselectivity, substrate scope, and yields (up to 92%). Mechanistically, redox-directed C–P bond cleavage and annulation were confirmed by a radical phosphonium path of the reaction. The intense fluorescence of the products can be regulated from blue to orange ( $\Phi_{\text{PLQY}}$  up to 77%). Importantly, modulated CPL was obtained for this series of emissive phosphahelicenes in a ternary cholesteric mesophase by chiral transmission, showing ultra-high asymmetry factors (+0.51, –0.48). Mechanistic study demonstrated that the increased CPL critically depended on chiral fluorescence resonance energy transfer (FRET) and helical superstructures rather than selective Bragg reflection.

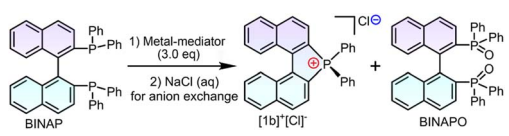
## Results and discussion

### Exploration of the C–P bond activation method and substrate scope

Inspired by the redox-related radical cation mechanisms in the annulation of redox-active Lewis acid mediators,<sup>40</sup> certain metal halide complexes have been predicted and chosen as targets. The corresponding diphosphines were acquired from commercial sources or prepared *via* the Monsanto method and characterized by NMR (nuclear magnetic resonance) and SCXRD (single crystal-XRD) (Fig. S2–S7 and Table S2†).<sup>41</sup> After metal-mediator screening in the presence of oxygen, a better yield of  $[\text{1b}]^+[\text{X}]^-$  was achieved with  $\text{MnCl}_2$  or  $\text{MnBr}_2$  at room temperature or under modest heating (complex counterions in the products were exchanged into chloride ions in brine), but was ineffective with  $\text{MnI}_2$  because of oxidative decomposition of iodide ions (Table 1, entries 1–5). Notably, the conversion speed of intramolecular cyclization was rapid under heating, which was faster than that at room temperature. In consideration of the conversion speed and yield, the reaction should be conducted at an elevated temperature ( $30\text{ }^{\circ}\text{C}$ ) for 5–10 minutes (entries 1–3). The presence of  $\text{O}_2$  could boost the reaction efficiency but inert argon inhibited the conversion (entry 1). Other non-halogenated  $\text{Mn}(\text{II})/\text{Mn}(\text{III})$  complexes led to negative results under the same conditions, generating BINAPO and the corresponding stable complexes (entries 6–9). The other metal halide candidates, *i.e.*,  $\text{FeCl}_3$ ,  $\text{CoCl}_2$ ,  $\text{NiCl}_2$ , and  $\text{CuCl}_2$ , are noneffective in this reaction (entries 10–13). All control experiments indicated that it was not only the redox potential for metal cations but also the halogen ion that displayed a unique efficacy in the reaction. Considering the polarity gap between substrates,  $\text{MnCl}_2$ , and ionic products, satisfactory conversion rates and isolated yields were obtained in the mixed solvents at  $30\text{ }^{\circ}\text{C}$  for  $[\text{1b}]^+[\text{Cl}]^-$  (entries 1 and 14–18).

Based on the optimized conditions in hand, the substrate scope was investigated for BINAPs/BIPHEPs (Scheme 2). Derivatives BINAP-4-Me and BINAP-3,5-Me<sub>2</sub> with methyl groups at different positions in phenyls converted into  $[\text{2b}]^+[\text{Cl}]^-$  and  $[\text{3b}]^+[\text{Cl}]^-$  with 54% and 56% yields. Partial BINAPs showed slow cyclization at room temperature due to lower activity, which required proper heating ( $50\text{--}80\text{ }^{\circ}\text{C}$ , Scheme 2). BINAPs with electron-donating methyl groups at *ortho*, *meta*, and *para*-positions converted into  $[\text{11b}]^+[\text{Cl}]^-$ ,  $[\text{12b}]^+[\text{Cl}]^-$ , and  $[\text{13b}]^+[\text{Cl}]^-$



Table 1 Screening of reaction conditions<sup>a</sup>


Entry	Mediator	Solvent	T (°C)	Yield <sup>c</sup> (%)
1	MnCl <sub>2</sub>	CHCl <sub>3</sub> : EtOH	30	56(37), ND <sup>e</sup>
2	MnCl <sub>2</sub>	CHCl <sub>3</sub> : EtOH	60	51(40)
3	MnCl <sub>2</sub>	CHCl <sub>3</sub> : EtOH	80	52(40)
4	MnBr <sub>2</sub>	CHCl <sub>3</sub> : EtOH	30	54(42)
5	MnI <sub>2</sub>	CHCl <sub>3</sub> : EtOH	30	Trace
6	MnCO <sub>3</sub>	CHCl <sub>3</sub> : EtOH	80	ND <sup>d</sup>
7	Mn(OTf) <sub>2</sub>	CHCl <sub>3</sub> : EtOH	80	ND <sup>d</sup>
8	Mn(acac) <sub>3</sub>	CHCl <sub>3</sub> : EtOH	80	ND <sup>d</sup>
9	Mn(OAc) <sub>3</sub>	CHCl <sub>3</sub> : EtOH	80	ND <sup>d</sup>
10	FeCl <sub>3</sub>	CHCl <sub>3</sub> : EtOH	80	ND <sup>d</sup>
11	CoCl <sub>2</sub>	CHCl <sub>3</sub> : EtOH	80	ND <sup>d</sup>
12	NiCl <sub>2</sub>	CHCl <sub>3</sub> : EtOH	80	ND <sup>d</sup>
13	CuCl <sub>2</sub>	CHCl <sub>3</sub> : EtOH	80	ND <sup>d</sup>
14	MnCl <sub>2</sub>	Toluene	80	Trace
15	MnCl <sub>2</sub>	Chloroform	80	38(35)
16	MnCl <sub>2</sub>	Ethanol	80	<5(11)
17	MnCl <sub>2</sub>	THF	80	42(47)
18	MnCl <sub>2</sub>	Acetonitrile	80	29(34)
19	MnCl <sub>2</sub> <sup>b</sup>	CHCl <sub>3</sub> : EtOH	30	Trace

<sup>a</sup> Reaction conditions: BINAP (0.16 mmol), metal-mediator (3.0 eq.).

<sup>b</sup> Mixed-solvent ( $V_{\text{chloroform}} : V_{\text{EtOH}} = 2 : 1$ , 10 mL), under an O<sub>2</sub> atmosphere (1 bar) at corresponding temperature for 5–10 minutes.

<sup>c</sup> 10 mol%. <sup>d</sup> Isolated yields for helicenes and BINAPOs (in parentheses). <sup>e</sup> ND represents not detected. <sup>f</sup> Ar instead of O<sub>2</sub>.

with depressed yields (37–42%), but the BINAPOs could be reduced and transformed into initial BINAPs by HSiCl<sub>3</sub> and utilized next time. Besides, ethyl, methoxyl, tertiary butyl, and mesitylene substituted BINAPs displayed higher yields (61–75%). Encouragingly, electron-deficient BINAPs (fluorine, trifluoromethyl, and ester) showed the highest yields (up to 85%). It was worth noting that the extensional phenyls, biphenyls, and naphthyls had an inconspicuous influence on intramolecular cyclization. Similarly, biphenyl diphosphines (BIPHEPs) cyclized into corresponding phosphoniums with moderate yields (39–67%). Unfortunately, the P,O-embedded phosphonium [8b]<sup>+</sup>[Cl]<sup>−</sup> did not generate in this reaction, which was related to the flexible aryl ether motion of the DPEPhos substrate and longer P–P distance (4.88 Å) than that of BINAP (4.20 Å), leading to a different chelation environment for the intermediate (Fig. S7†). Furthermore, 5,5′-modified BINAPs showed satisfactory tolerance (40–73%) equal to those of 6,6′-modified BINAPs. Nevertheless, the 7,7′-modified BINAPs exhibited excellent cyclization, getting the highest yields (68–92%) of phospho[5]helicenes, which could be relevant to variational electronic structures and an elevated competitive rate between cyclization and oxidation. Finally, gram-scale reactions were performed with good yields (Scheme 2). To the best of our knowledge, this method represented the first C–P bond activation discovery in diphosphines using non-noble metal

mediators. This family of helicenium products could be transformed into asymmetric monophosphines by Pd-catalyzed stereoselective cleavage of the C–P bond and cross-coupling according to a recent report.<sup>23</sup>

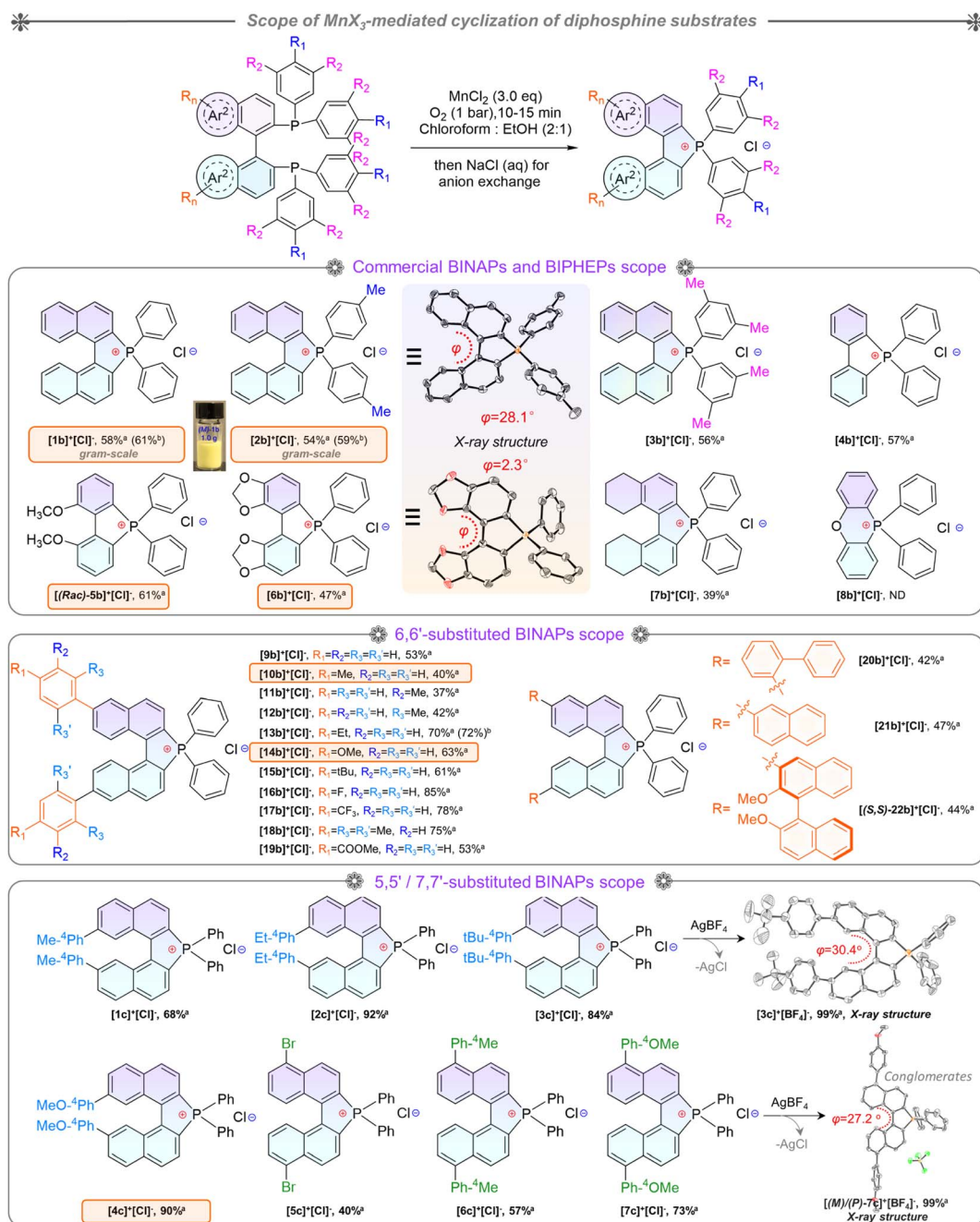
Indeed, this cyclization was highly stereospecific, where the product chirality inherited the BINAPs. However, the enantiomeric purity decreased in solution due to a low interconversion barrier at room temperature.<sup>23,42</sup> Enantiomerically enriched [2b]<sup>+</sup>[Cl]<sup>−</sup> and [2b]<sup>+</sup>[BF<sub>4</sub>]<sup>−</sup> were acquired *via* rapid synthesis, chromatographic purification, and their single-crystal growth at low temperature to guarantee adequate enantiomeric purity. Combined with the observations of SCXRD and uniform morphologies (Fig. S8, S9, S16, S17, and S21†), these proofs affirmed the formation of homochiral single crystals. The homochiral crystals were used for the kinetic study of chirality. Initially, we attempted to evaluate the ee values of compounds using chiral HPLC (at 25 °C) but failed. To this end, we then employed the temperature and time-dependence of the rate constant to calculate the ee values and thermodynamic parameters of the racemization process *via* CD (circular dichroism) spectra (see the ESI for detailed determination, Fig. S1†). According to the CD ellipticities between homochiral crystals and pristine products in solution, the average ee value (for 5 parallel samples) of pristine product [2b]<sup>+</sup>[Cl]<sup>−</sup> was about 73%. Finally, as a summary of Eyring plotting and calculations for [2b]<sup>+</sup>[Cl]<sup>−</sup>,  $\Delta H^\ddagger = 12.5 \text{ kcal mol}^{-1}$  and  $\Delta S^\ddagger = -25.4 \text{ cal mol}^{-1} \text{ K}^{-1}$  were determined, and  $\Delta G^\ddagger_{\text{exp}} = 20.1 \text{ kcal mol}^{-1}$ ,  $k = 1.5 \times 10^{-4} \text{ s}^{-1}$ , and  $t_{1/2}$  (half-life) = 77.1 min at 298.15 K were successfully elucidated, whose  $\Delta G^\ddagger_{\text{exp}}$  value was smaller than that of carbon[5]helicene ( $\sim 25 \text{ kcal mol}^{-1}$  at 298.15 K).<sup>43–45</sup> The  $\Delta G^\ddagger_{\text{exp}}$  value was slightly below the margin of the activation barrier ( $\sim 22.2 \text{ kcal mol}^{-1}$ ) required for conformational atropo-enantiomers to be resolvable.<sup>46</sup> In addition, the interconversion of helical conformation was also considered *via* density functional theory (DFT) calculations, and the isomerization crossed over the saddle-shaped transition state with a low isomerization barrier ( $\Delta G^\ddagger_{\text{cal}} = 24.1 \text{ kcal mol}^{-1}$ , at the B3LYP/6-31G\* level) of [(P)/(M)-2b]<sup>+</sup> (Fig. S38†). The degraded ee value observed in our experiments was reasonable, and the experimental  $\Delta G^\ddagger_{\text{cal}}$  value was smaller by 4.0 kcal mol<sup>−1</sup> than the theoretical one. The reason for the latter may be the problem of the accuracy of the basis set/functionality.<sup>47</sup> The lower  $\Delta G^\ddagger_{\text{cal}}$  18.6 kcal mol<sup>−1</sup> of [(P)/(M)-1b]<sup>+</sup> facilitated the loss of stereochemical purity completely and the heterochiral crystal packing pattern (Fig. 4g). Consequently, (P)-[2b]<sup>+</sup> manifested homochiral crystallization, which could inherit (S)-BINAP handedness and higher stability (Fig. S38†). The robust isomerization barriers and well-tailored D–A modules of phospho[5]helicene cations could be realized by introducing strong electron donors at 7,7′/8,8′-positions, and this project was still in progress.

### Mechanistic studies by control experiments and DFT calculations

Control experiments and calculations were performed to understand the reaction mechanism (Scheme 3a). First, the cyclization showed no conversion using the catalytic amount of





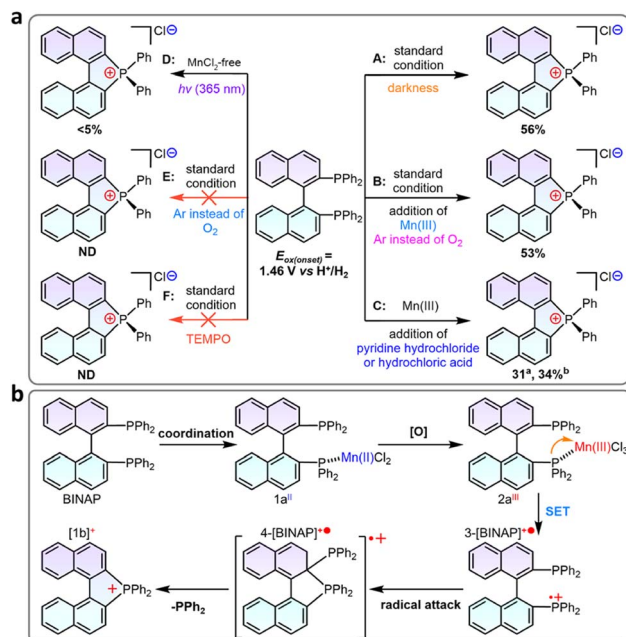


**Scheme 2** Diphosphine scope of intramolecular cyclization. Reaction conditions: diphosphines (0.2 mmol),  $\text{MnCl}_2$  (3.0 eq.), mixed-solvent (10 mL), under an  $\text{O}_2$  atmosphere (1 bar) at corresponding temperature for 10 minutes. Corresponding reaction temperatures: 30 °C: [1b]<sup>+</sup>[Cl]<sup>−</sup>–[3b]<sup>+</sup>[Cl]<sup>−</sup>, 50 °C: [4b]<sup>+</sup>[Cl]<sup>−</sup>–[7b]<sup>+</sup>[Cl]<sup>−</sup>, [9b]<sup>+</sup>[Cl]<sup>−</sup>–[18b]<sup>+</sup>[Cl]<sup>−</sup>, and [1c]<sup>+</sup>[Cl]<sup>−</sup>–[7c]<sup>+</sup>[Cl]<sup>−</sup>, and 80 °C: [8b]<sup>+</sup>[Cl]<sup>−</sup>; [20b]<sup>+</sup>[Cl]<sup>−</sup>–[22b]<sup>+</sup>[Cl]<sup>−</sup>. <sup>a</sup>Isolated yields of the 0.2 mmol-scale reaction. <sup>b</sup>Isolated yields of the gram-scale reaction.

$\text{MnCl}_2$  (10 mol%, entry 19), indicating that excess counterions from  $\text{MnCl}_2$  were essential for the charge balance in the ionic product. The cyclization was suppressed in argon, which could be related to the redox process in the reaction. To gain more insight into this speculation, we conducted  $\text{Mn(III)}$ -prompted studies in the presence of necessary counterionic chloridions (HCl or pyridine hydrochloride). The  $\text{Mn(III)}$  ion possessed appropriate oxidizing power ( $E_{\text{red}} = 1.51 \text{ V}$ , vs.  $\text{H}^+/\text{H}_2$ ) and can oxidize the BINAP ( $E_{\text{ox(onset)}} = 1.46 \text{ V}$  vs.  $\text{H}^+/\text{H}_2$ , Fig. S22†) to give

radical phosphonium and cyclization products. The reduction potential of the metal complexes was crucial to this cyclization, as demonstrated by the high reactivity of activated  $\text{Mn(III)Cl}_3$  in contrast to the lack of reactivity of  $\text{Fe}^{3+}$  (0.77 V),  $\text{Co}^{2+}$  (0.28 V),  $\text{Ni}^{2+}$  (−0.23 V), and  $\text{Cu}^{2+}$  (0.16 V) in the reaction. Indeed, when  $\text{Mn(OAc)}_3$  was injected into a mixture of BINAP and  $\text{MnCl}_2$  under inert Ar conditions, the mixture also underwent rapid oxidation and cyclization to form [1b]<sup>+</sup>, indicating that *in situ*  $\text{Mn(III)Cl}_3$  triggered the single electron transfer from the P-atom





Scheme 3 (a) Control experiments of the reactions. (b) Plausible mechanism.

to Mn(III) (Scheme 3a). Unexpectedly, photocyclization took place in the absence of MnCl<sub>2</sub> under UV radiation in the air with a meager yield but increased moderately with the addition of counter chloridions (HCl or pyridine hydrochloride, yields from 3% to 14%), suggesting the homolysis of the C–P bond in the photoinduced excited state (Scheme 3a, Fig. S24†). Other low-energy light sources (405 nm or indoor light) cannot activate cyclization owing to the unmatched absorption energy of BINAP (Fig. S25†). Furthermore, both standard MnCl<sub>2</sub>-mediated and photo-induced annulations were suppressed in radical scavenger TEMPO. These results concluded that the intramolecular cyclization proceeded *via* a radical pathway.<sup>20</sup> Furthermore, the dark experiments had a similar cyclization yield to the MnCl<sub>2</sub>-mediated system (Scheme 3a).

The DFT calculated HOMO of BINAP revealed that electrons were dominated on the P-moieties (Fig. 1a), giving the preferential oxidation of losing one electron in the P-atom and generating the corresponding radical cation 3-[BINAP]<sup>•+</sup> after single electron transfer (SET) oxidation by Mn(III)Cl<sub>3</sub>. Spin densities analysis demonstrated that P-atoms had the highest spin densities in radical cation 3-[BINAP]<sup>•+</sup> and were preferred sites for the radical attack (Fig. 1a). The calculated Gibbs free energies of the critical transition states also supported the observation that phosphonium attack at the C2'-position was favorable with a low barrier ( $\Delta G^\ddagger = 19.8 \text{ kcal mol}^{-1}$ , Fig. 1b), which was reasonable for the observed mild cyclization conditions at near room temperature. With the above results and previous studies on metal-triggered cleavage and annulation of C–P bonds in hand, a plausibly radical phosphonium pathway is depicted in Scheme 3b.<sup>16,50–53</sup> The preferential coordination of BINAP with MnCl<sub>2</sub> formed an Mn(BINAP)Cl<sub>2</sub> intermediate (1a), after which the presence of oxygen caused the oxidation of

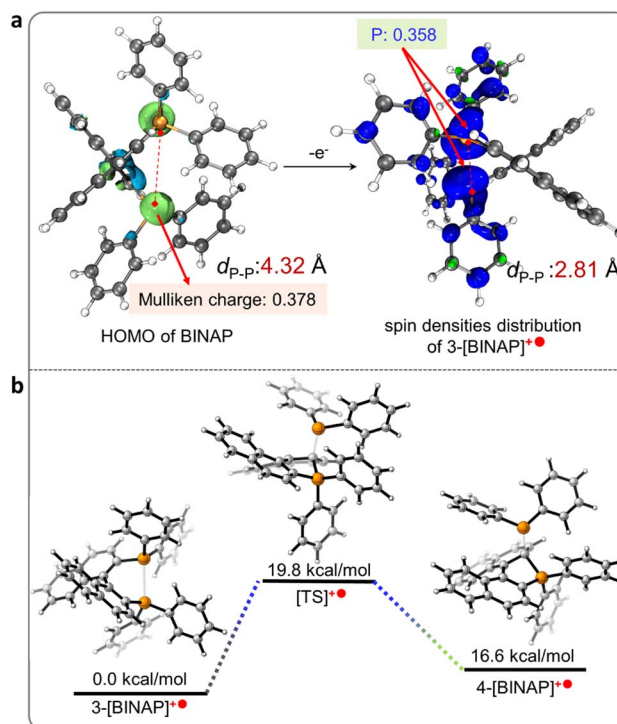


Fig. 1 (a) DFT calculated HOMO diagrams and Mulliken charge of the substrate BINAP (left), and spin densities of radical phosphonium of 3-[BINAP]<sup>•+</sup> (right). (b) Calculated Gibbs free-energy diagrams of the formation of a five-membered ring *via* the radical phosphonium pathway.

Mn(II) to Mn(III) complexes (2a). The matched redox potential in the Mn(III) complex led to the formation of radical phosphonium 3-[BINAP]<sup>•+</sup> *via* the SET oxidation between the P-atom and Mn(III)-center. The subsequent attacks with the C2'-position produced the cyclized radical cation 4-[BINAP]<sup>•+</sup>, which eliminated the PPh<sub>2</sub> residue to form thermodynamically stable [1b]<sup>+</sup>.<sup>54,55</sup>

### Crystallographic structure determination

Single crystals of enantiomeric and racemic [2b]<sup>•+</sup>[X]<sup>–</sup> were grown from the purified compounds by slow volatilization in mixed solvents (details are listed in the ESI†). [(6b)<sup>•+</sup>]<sub>2</sub>[MnCl<sub>4</sub>]<sup>2–</sup> crystals were obtained from the reaction mixtures in Schlenk tubes after slow cooling and volatilization. [(M)-2b]<sup>•+</sup>[Cl]<sup>–</sup>, [(P)-2b]<sup>•+</sup>[Cl]<sup>–</sup>, and [(P)-2b]<sup>•+</sup>[Br]<sup>–</sup> crystallized in the chiral *P*<sub>2</sub><sub>1</sub><sub>2</sub><sub>1</sub> space group with regular cuboid morphology (Fig. 2j and S8–S10†). For [(M)-2b]<sup>•+</sup>, the quaternary P-atom occupied the center and coordinated with chiral binaphthyl and 4-tolyl wings to form a distorted tetrahedron topology, where the C–P bond lengths were determined to be 1.76–1.79 Å, which were close to DFT optimized values (1.79–1.80 Å) and shorter than those of precursor BINAPs (1.83–1.85 Å, Fig. 2a). The bond angle of  $\varphi(\text{C}_{11}\text{P}_1\text{C}_{12})$  was 94.6° in the five-membered ring, which was smaller than that of the opposite unclosed wing  $\varphi(\text{C}_{21}\text{P}_1\text{C}_{28})$  (114.0°). The selected dihedral angle ( $\theta$ ) for the binaphthyl unit and torsion angle ( $\varphi$ ) for the binaphthyl axis were determined at



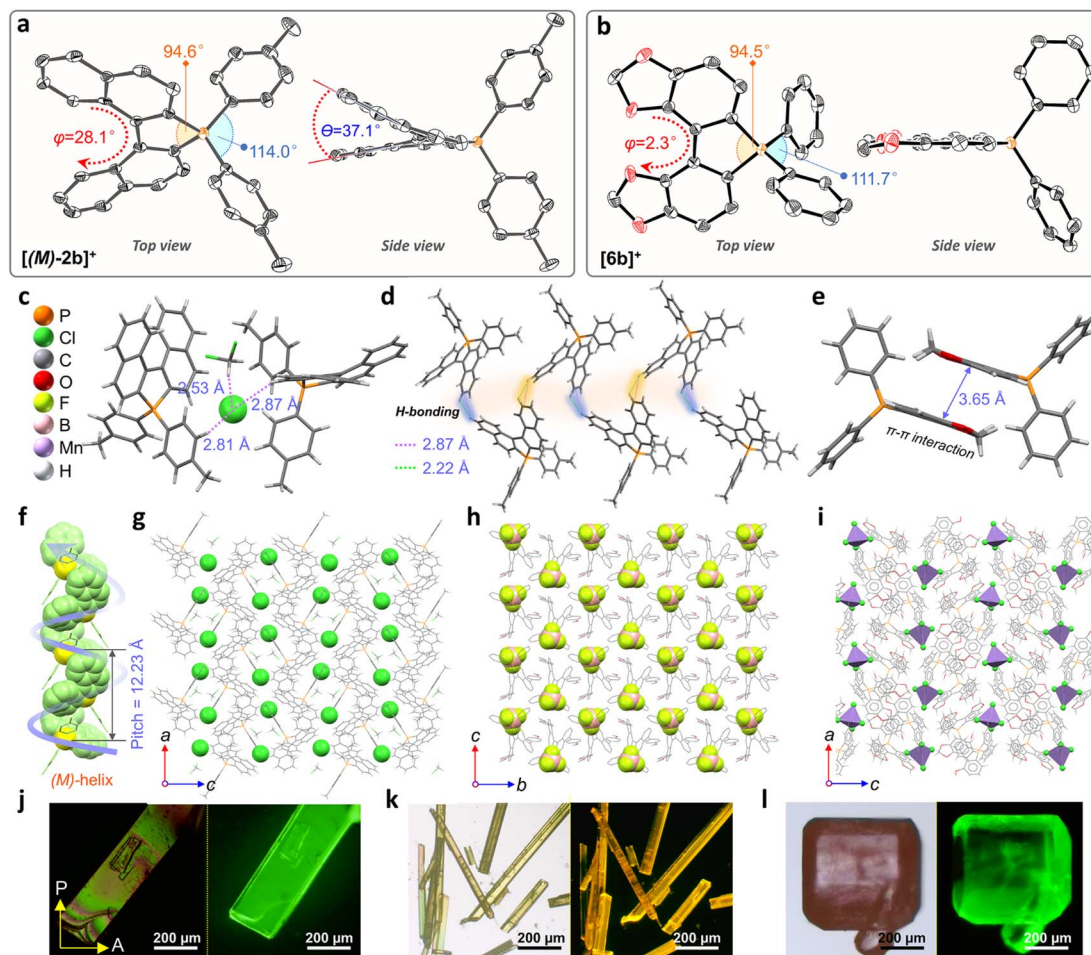


Fig. 2 (a) ORTEP drawing of  $[(M)-2b]^+[Cl]^-$  and (b) complex  $[6b]^+[MnCl_4]^{2-}$  with thermal ellipsoids set at the 50% probability level. The hydrogen atoms, solvents, and anions are omitted for clarity. (c) Multiple H $\cdots$ Cl bonding interactions between two molecules and  $CH_2Cl_2$  of  $[(M)-2b]^+[Cl]^-$ . (d) Interlaced hydrogen bonding interactions in adjacent molecules of  $[(M)-2b]^+[Cl]^-$ . (e) Dimeric packing of  $[6b]^+$  units in  $[(6b)^+]_2[MnCl_4]^{2-}$ . (f and g) Crystal packing of  $[(M)-2b]^+[Cl]^-$  and (h)  $[(M)-7c]^+[BF_4]^-$  and (i)  $[(6b)^+]_2[MnCl_4]^{2-}$  complexes. (j) Polarized optical microscope (left) and fluorescence microscope images (right, excited at 365 nm) of  $[(M)-2b]^+[Cl]^-$  and (k)  $[(M)-7c]^+[BF_4]^-$  crystals. (l) Bright-field optical microscope (left) and fluorescence microscope images (right, excited at 365 nm) of  $[(6b)^+]_2[MnCl_4]^{2-}$  crystals.

37.1° and 28.1° due to steric hindrance at the 8,8'-positions of hydrogen atoms (Fig. 2a). This structural constraint should cause a compression of left-handedness helicity (absolute configuration was confirmed using a reliable flack parameter of 0.03(5), Table S3†), where the dihedral angle ( $\theta = 37.1^\circ$ ) of  $[(M)-2b]^+$  was reduced to about 44.9° compared with that of BINAPs ( $\theta = 82.0^\circ$ ).  $[(M)-2b]^+[Cl]^-$  crystals were acquired from the (*R*)-BINAPs precursor, while  $[(P)-2b]^+[Cl]^-$  was derived from (*S*)-BINAPs, which demonstrated that stereochemistry might be preserved throughout the preparation and crystallization. The nonplanar tetrahedron backbone interrupted  $\pi$ - $\pi$  interactions, but multiple H $\cdots$ Cl bondings (2.53–2.87 Å) existed between adjacent ionic pairs as well as  $CH_2Cl_2$  solvent, and the chloridions were restricted in the voids by cationic helicenes (Fig. 2c and g). The homochiral blocks were linked by the strongly interlaced H-bonds (Fig. 2d). However, the racemic  $[(\text{Rac})-2b]^+[Br]^-$  crystallized in the centrosymmetric  $C2/c$  space group with a long rhomboid shape and exhibited obvious H $\cdots$ Br interactions (2.46–2.97 Å) between neighboring ionic pairs.

Therefore, this affirmed that the installation of a quaternary P-atom embedded at the helical tetrahedron can result in large steric resistance that destroys the  $\pi$ -stacking of phosphahelicenes (Fig. S21†). Notably, all ionic crystals emitted intense fluorescence, distinct from weakly emissive trivalent phosphahelicenes and their oxides (1 and 2 are nonemissive, Scheme 1c).<sup>16</sup> Importantly, 0-D hybrid  $[(6b)^+]_2[MnCl_4]^{2-}$  crystals were captured in the reaction mixture, and the organic cation  $[6b]^+$  exhibited a distinguishing construction compared to  $[(P)-2b]^+$  (Fig. 2b, i, and l). The flat 4,4'-bibenzo[*d*][1,3]dioxole unit ( $\theta = 0^\circ$ ,  $\varphi = 2.2^\circ$ ) adopted horizontal conformation due to inexist steric hindrance of dioxole units, where flat rings favored the formation of strong H-bonding (2.55–2.60 Å) and  $\pi$ - $\pi$  (3.65 Å) interactions in antiparallel dimers (Fig. 2i and S12b†), demonstrating that chirality was annihilated in  $[6b]^+$ . The computationally reduced density gradient (RDG) maps using DFT calculations revealed direct intermolecular noncovalent interactions (NCIs) between dimers as well (Fig. S12d†).<sup>56</sup> Interestingly, the crystals of  $[(6b)^+]_2[MnCl_4]^{2-}$  emitted intense green





phosphorescence at 511 nm owing to the  $4T^1(G) \rightarrow 6A^1$  radiative decay in  $[MnCl_4]^{2-}$ , but  $[6b]^+[Cl]^-$  allowed deep blue fluorescence (Fig. 2l, 5d, and S46†). This fact suggested that the excited energy transfer between  $[MnCl_4]^{2-}$  and donor  $[6b]^+$  in the rigid crystal could be beneficial for generating sensitized phosphorescence because of their appropriate energy levels.<sup>57,58</sup>

As mentioned above, the installation of the diverse anions at the ionic crystals of phosphahelicenes can bring out robust NCI in the packing of those molecules. This might also explain well why our devotion to growing single crystals of other phosphahelicenes (the small halide ion acted as the counterion) ultimately failed, since a more torsional aromatic substituent at the edge-position might significantly result in loose stacking and an unfitting cavity of molecules during the crystallization process. Therefore, the large anion exchange strategy was tried to obtain high-quality single crystals to gain insight into structural information on crystallizing-induced assembly and chiral character. As expected, a series of single crystals were obtained by anion exchange in equivalent halide scavenger ( $AgBF_4$  or  $AgPF_6$ ) solutions.  $[Cl]^-$  anions in enantiomerically enriched  $[(P)-2b]^+[Cl]^-$  and  $[(M)-2b]^+[Cl]^-$  could be exchanged with  $[BF_4]^-$  or  $[PF_6]^-$  anions smoothly, while the crystallographic and stereochemical information was maintained (Fig. S16 and S17†), indicating that the initial chiral bias of cations could be inherited and racemization was hindered during the recrystallization.<sup>59,60</sup> In contrast, the prepared  $[1b]^+[BF_4]^-$  and  $[1b]^+[PF_6]^-$  crystals bearing the  $PPh_2$  moieties exhibited expected heterochiral arrangements regardless of stereochemical conformation for precursors (Fig. S14 and S15†). This result demonstrated the racemic nature of the prepared  $[1b]^+[Cl]^-$  under the same conditions, where the isomerization barrier was lower than that of  $[2b]^+[Cl]^-$  by about  $5.5 \text{ kcal mol}^{-1}$  (Fig. 4g and S38†). In  $[(Rac)-3c]^+[BF_4]^-$ , two edge aromatic rings suffered from folded orientation, huge repulsion, and distortion, thus severely enlarging their dihedral angle for the binaphthyls ( $\theta = 43.6^\circ$ ) and edge phenyls ( $\theta' = 72.9^\circ$ ) as well as the persistence of chiral configuration. In addition, the (*M*)-isomer or (*P*)-isomer accumulated into 1-D columnar superhelicenes along the *b*-axis with opposite handedness *via* tight  $\pi$ - $\pi$  stacking ( $3.42$ – $3.87 \text{ \AA}$ ) and alternate rotation about  $81^\circ$  and  $99^\circ$  (Fig. 3a and S18g†), where the helical pitch was  $23.96 \text{ \AA}$ . Unexpectedly, homochiral  $[(M)-7c]^+[BF_4]^-$  and  $[(P)-7c]^+[BF_4]^-$  conglomerates were crystallized in racemic solutions (Fig. 3b), but this chiral self-sorting tendency has not been observed in  $[(Rac)-3c]^+[BF_4]^-$ ,  $[(Rac)-1b]^+[BF_4]^-$ , and  $[(Rac)-1b]^+[PF_6]^-$ , manifesting that the chiral self-discrimination was dependent on the subtle variation of cations (Fig. S14, S15, S18, and S19†).<sup>60</sup>

### Aromaticity analysis

The quaternary C–P bonding environment and electron-deficient nature of the P-center might bring out unique electronic structures. First, the aromaticity of the skeleton was investigated by anisotropy of the induced current density (AICD) and nucleus independent chemical shifts (NICS) simulations (Fig. 4a–f).<sup>61,62</sup>  $[(P)-2b]^+$  manifested a diatropic ring current originating from a binaphthyl fragment along the periphery of

the helical backbone (Fig. 4a), but the current was broken between the binaphthyl unit and phenyl wings at the penta-heterocycle due to the tetrahedral P(III)-node, confirming the local aromaticity in  $[(P)-2b]^+$ .  $[(R)-5b]^+$  and  $[(P)-14b]^+$  had similar aromaticity as well (Fig. 4b and c). NICS analysis was adopted to gain a degree of theoretical aromaticity for  $[(P)-1b]^+$  and others (Fig. 4d–f). The negative NICS values revealed typical aromaticity in binaphthyl (NICS(0):  $-7.6 \text{ ppm}$  and  $-9.0 \text{ ppm}$ ) and phenyl rings ( $-8.4 \text{ ppm}$ ) but antiaromaticity in the P(III) penta-heterocycle (NICS(0):  $+3.8 \text{ ppm}$ , NICS(1):  $+2.1 \text{ ppm}$ ), which was consistent with the broken AICD at the P(III)-node. The local aromaticity was similar to that of other azahelicenes (anti-aromaticity for heteroatomic linking rings) but different from that of carbohelicenes and O/S-atom embedded ones (global aromaticity).<sup>63–65</sup>

### Electronic structures and photophysical properties

Electronic absorption spectra of synthetic compounds are shown in Fig. 5a, S40, and S42.† Representative systems were discussed (structures highlighted in Scheme 2) in this section and others are analyzed in the ESI.†  $[1b]^+[Cl]^-$  gave a strong absorption band from 225 to 310 nm and two weak shoulder peaks at 330 and 412 nm (Fig. 5a). TD-DFT calculations showed that the absorption band of  $[1b]^+$  in the longest wavelength region was attributed to the HOMO  $\rightarrow$  LUMO transition (98.8%,  $f = 0.118$ , Fig. 5b, S29, and Table S9†). The electronic cloud was mainly distributed on binaphthyl for the HOMO, while the LUMO electronic cloud was primarily located on the binaphthyl and electron-deficient P(III)-pentagon, indicating locally excited (LE) characteristics in  $[1b]^+$  (Fig. 4h).  $[5b]^+[Cl]^-$  and  $[6b]^+[Cl]^-$  experienced identifiable hypsochromic shifted absorption with similar LE characteristics due to the reduced conjugated backbone, but extended phosphahelicenes ( $[9b]^+[Cl]^-$ – $[21b]^+[Cl]^-$ ) at 6,6'-positions displayed a similar absorption curve and enhanced absorbance (Fig. 5a and S40†). The variation tendency of the optical bandgap agreed well with the computational orbital gaps ( $\Delta E = E_{\text{LUMO}} - E_{\text{HOMO}}$ , Fig. 4h). Interestingly, the LE transition was gradually transformed into the intramolecular charge transfer (ICT) state for  $[(P)-10b]^+$ ,  $[(P)-7c]^+$ ,  $[(P)-14b]^+$ ,  $[(P)-4c]^+$ , and  $[(P)-18b]^+$  owing to the torsional electron donor, which could be confirmed by the separated electronic cloud in the HOMO and LUMO.<sup>36,37</sup> The HOMO-electrons resided on the extended phenyls, and the LUMO-electrons were dominated by the P(III)-pentagon with high contributions up to 46.8–48.2% (8.3–8.5% on the P-atom, Fig. S35†), suggesting a typical electron-deficient character of the quaternary bonding scaffold, which was distinct from the typical LE nature of trivalent and pentavalent phosphahelicenes.<sup>29,31,66</sup> Solvent-dependent UV-vis absorption and fluorescence emission reaffirmed the mutation of LE to ICT of  $[(P)-14b]^+[Cl]^-$  due to the torsional D–A structure and elevated transition dipole moments (Fig. S45†).<sup>67</sup>

Remarkably, all compounds were emissive in chloroform and solid states.  $[1b]^+[Cl]^-$  exhibited structureless green emission at 498 nm with moderate PLQY ( $\Phi = 21\%$ ) in chloroform (Fig. 5b). TD-DFT calculations suggested that the fluorescence



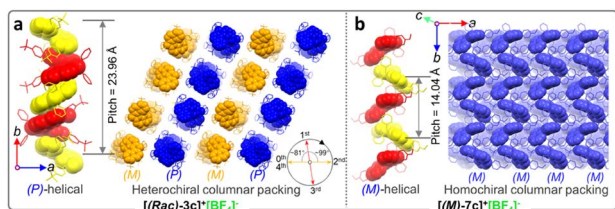


Fig. 3 (a) Crystal structure arrangements of  $[(Rac)-3c]^+ [BF_4]^-$  and (b)  $[(M)-7c]^+ [BF_4]^-$ . The hydrogen atoms and anions are omitted for clarity.

showed the  $S_1 \rightarrow S_0$  transition (Fig. 5b). Moreover, the emission of  $[1b]^+ [Cl]^-$  powder displayed a slight bathochromic shift together with a retentive full width at half maximum (FWHM = 76 nm) and an enhanced PLQY ( $\Phi = 34\%$ ) owing to the rigidity-enhanced environment in the solid and restriction of intramolecular rotation (RIR) of the tetrahedral C–P scaffolds.<sup>68</sup> Furthermore, the fluorescence could be adjusted from deep

blue to orange for these serial emitters, including deep blue  $[6b]^+ [Cl]^-$ , 405 nm,  $\Phi = 12\%$ , sky blue  $[5b]^+ [Cl]^-$ , 457 nm,  $\Phi = 77\%$ , yellow  $[2c]^+ [Cl]^-$ , 540 nm,  $\Phi = 39\%$ , orange-yellow  $[14b]^+ [Cl]^-$ , 560 nm,  $\Phi = 35\%$ , and orange  $[4c]^+ [Cl]^-$ , 568 nm in the solid state,  $\Phi = 47\%$  (Fig. 5c, S41, S43, and Table S12†). Their fluorescence lifetimes ( $\tau$ ) varied from 1.7 to 12.9 ns in chloroform (Fig. 5d). The longer decay of  $[14b]^+ [Cl]^-$  and  $[4c]^+ [Cl]^-$  than  $[1b]^+ [Cl]^-$  could be interpreted as slower relaxation kinetics in the ICT state.<sup>67</sup> Notably, all methoxy-substituted compounds at different positions exhibited significant Stokes shifts and higher quantum efficiency, which can be attributed to the enhanced ICT feature of the D–A structures, as evidenced by electronic donation and communication of the bridge methoxy group (Tables S10, S12, and Fig. S32a†).

### Chiroptical properties and chiral induced LC self-assembly

Solid chiroptical properties of enantiomerically enriched  $[2b]^+ [Cl]^-$  and  $[2b]^+ [BF_4]^-$  crystals were evaluated at room

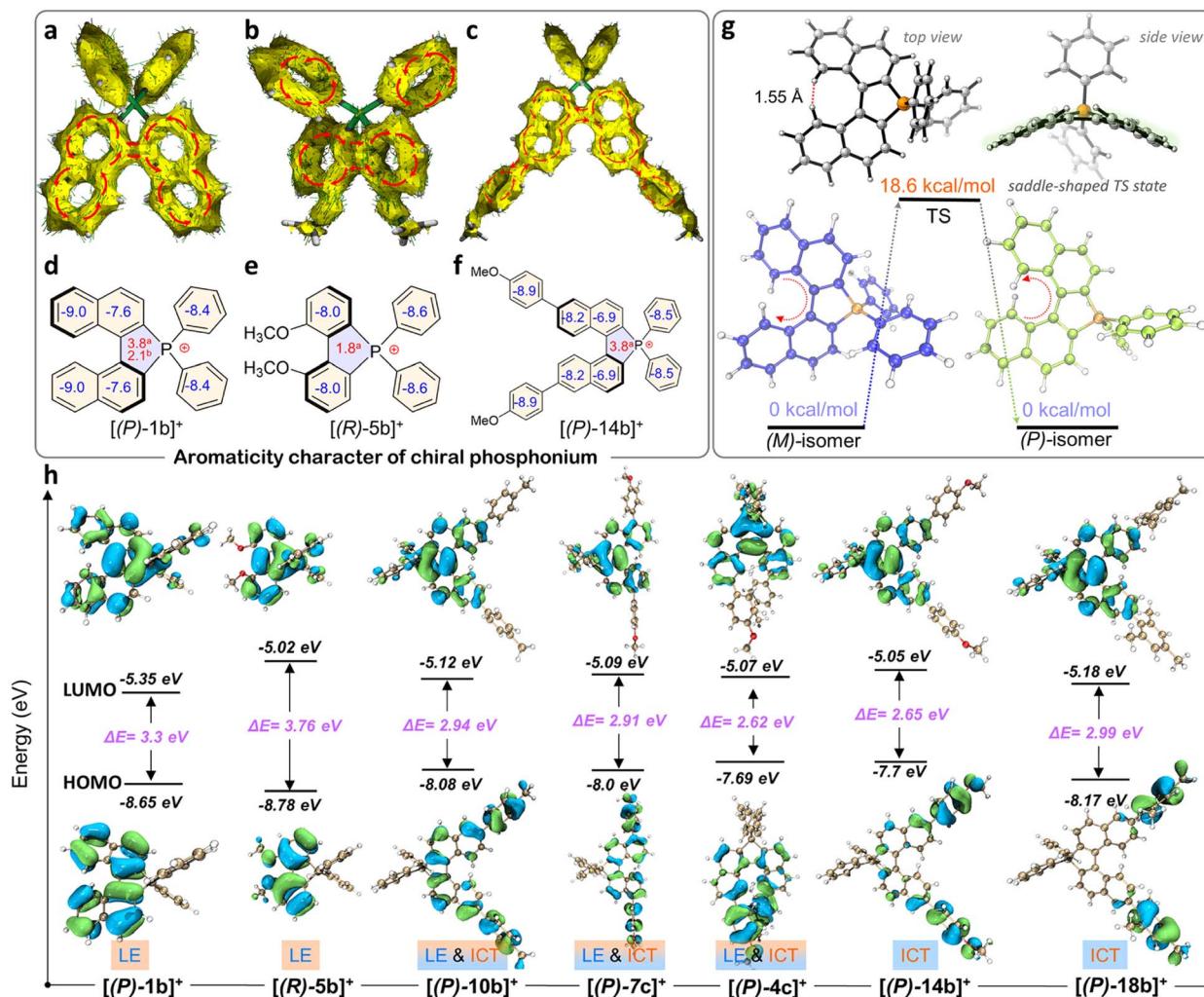


Fig. 4 (a–c) DFT calculated AICD plots of  $[(P)-1b]^+$ ,  $[(R)-5b]^+$ , and  $[(P)-14b]^+$  at the CSGT-B3LYP/6-31G(d) level. The red arrows indicate ring current delocalized along the aromatic rings. (d–f) DFT calculated  $^a\text{NICS}(0)$  and  $^b\text{NICS}(1)$  values of  $[(P)-1b]^+$ ,  $[(R)-5b]^+$ , and  $[(P)-14b]^+$  at the GIAO-B3LYP/6-31G(d) level. (g) Calculated racemization barrier ( $\Delta E^\ddagger$ ) and conformation for cation  $[1b]^+$  between the (M)-isomer and (P)-isomer at the B3LYP/6-31G(d) level. (h) Frontier molecular orbital diagrams and energy gaps ( $\Delta E$ ) for representative phosphonium (B3LYP/6-311G(d) level).





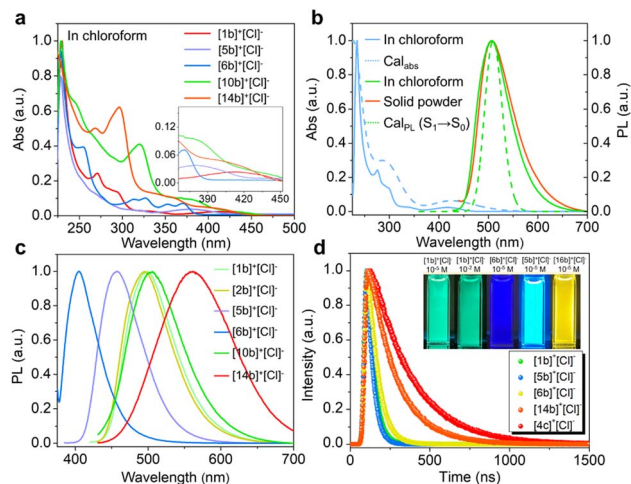


Fig. 5 (a) Normalized UV-vis spectra of compounds  $[1b]^+[Cl]^-$ ,  $[5b]^+[Cl]^-$ ,  $[6b]^+[Cl]^-$ ,  $[10b]^+[Cl]^-$ , and  $[14b]^+[Cl]^-$  in chloroform with  $2 \times 10^{-5}$  M at room temperature. (b) Experimental and TD-DFT simulated UV-vis and PL spectra of  $[1b]^+[Cl]^-$ . (c) PL spectra of the representative compounds in chloroform with  $1 \times 10^{-4}$  M at room temperature ( $\lambda_{ex} = 370$  nm for  $[1b]^+[Cl]^-$ ,  $[2b]^+[Cl]^-$ ,  $[10b]^+[Cl]^-$ , and  $[14b]^+[Cl]^-$  and 360 nm for  $[5b]^+[Cl]^-$  and  $[6b]^+[Cl]^-$ ). (d) Transient fluorescence decay curves for selective compounds in chloroform ( $1 \times 10^{-4}$  M) and their photographs under UV-light.

temperature. The enantiomerically enriched  $[2b]^+[BF_4]^-$  crystals afforded mirrored CD signals from 280 to 450 nm (Fig. 6a). However, the solution CD intensity deteriorated quickly at the room temperature of kinetic experiments (Fig. S1 and S48a†). The CPL activity of the solution was observed with moderate dissymmetry factors ( $\pm 0.94 \times 10^{-3}$ ) and decreased with increased radiation time and temperature, indicating loss of enantiomeric purity (Fig. S48c and S48d†).

CPL spectra were also collected for crystalline  $[(M)/(P)-2b]^+[BF_4]^-$  powder (Fig. 6 and S44†). Angle-dependent CD/CPL (enantiomerically enriched crystals) and extra CPL (racemic crystals) measurements were performed. CD/CPL signs were unchanged when altering the rotation angles, confirming that the contributions of birefringence and linear dichroism to the CD signals were negligible and the resultant chiral spectra were reliable (Fig. S49†). Enantiomerically enriched  $[2b]^+[BF_4]^-$

microcrystals exhibited mirrored CPL emission at 496 nm with moderate luminescence dissymmetry factors ( $g_{lum}$ ) of  $3.3 \times 10^{-3}/-3.5 \times 10^{-3}$ , which originated from  $S_1 \rightarrow S_0$  emission. The experimentally negative CPL signal of  $[(P)-2b]^+[BF_4]^-$  was consistent with the TD-DFT simulative results (Fig. S45b, see the ESI† for detailed determination). The  $|g_{lum(exp)}|$  values and PLQY (41%) for  $[(P)/(M)-2b]^+[BF_4]^-$  were comparable to those of reported carbo[n]helicenes and heterohelicenes,<sup>69</sup> and the order of magnitude was also equivalent to those of pentavalent phosphahelicene oxides.<sup>29,31,66</sup> These results reaffirmed that the synergistic construction of a quaternary C–P bonding environment and helical skeleton was an efficient way to prepare CPL active phosphahelicenes.

Controlling dynamic chirality expression is a formidable challenge and an attractive project for prochiral emitters (their chiral conformation only remained at the condensed phase), for instance, propeller-like TPE derivatives,  $C_3$ -symmetric dendrimers, axial atropisomers, and macrocycles.<sup>70,71</sup> The dynamic chiral conformation in [5]helicenes may be further controlled and induced,<sup>38,39</sup> but this conjecture has not been illustrated at present in phosphahelicenes. Herein, an attempt has been made to address this issue through chiral induced LC self-assembly for phosphahelicenes. First, we designed and synthesized a pair of axial chiral guests-A ( $(R)/(S)$ -BINOL-CN) and guests-B (phospha[5]helicenes) and screened for compatibility and helical twist power (HTP) between the LC host (5CB) and guests (Fig. 7a and b). A ternary cholesteric LC system has been prepared by annealing of the polar 5CB host, racemic phosphorus[5]helicenes (2.0 wt%,  $[6b]^+[Cl]^-$  or  $[2c]^+[Cl]^-$  or  $[4c]^+[Cl]^-$ ), and chiral BINOL-CN (0.5–4.0 wt%) mixtures (details are listed in the ESI†). Pure 5CB exhibited a Schlieren texture in the traditional nematic phase at room temperature under a polarized optical microscope (POM), while a uniform fingerprint texture was observed in ternary cholesteric LCs with periodic helicity (Fig. 7c and d). As the concentration of  $(S)$ -BINOL-CN increased, the average helical pitch of the fingerprint gradually decreased (Fig. S60 and S61†). Finally, the fingerprint texture transformed into an oily streak texture (4.0 wt%), where the XRD diffraction peak was absent in the small-angle region (Fig. S61e†), confirming that the orientational helical superstructures were induced.<sup>72,73</sup>

CD spectra of the cholesteric LC film doped with fixed contents of emitters (2.0 wt%) and  $(S)/(R)$ -BINOL-CN (4.0 wt%) are shown in Fig. 7e. All prepared  $(S)-N^*$  and  $(R)-N^*$  films produced strong negative and positive CD signals at 300–500 nm with large  $g_{abs}$  ( $-0.24$  to  $-0.37$ ,  $+0.21$  to  $+0.36$ ), respectively. The corresponding CPL spectra of enantiomeric LC films ( $4c-N^*$ ) revealed high  $g_{lum}$  at 549 nm, up to  $(+0.51, -0.48)$ , while the enantiomeric  $2c-N^*$  and  $6b-N^*$  LC films exhibited slightly lower  $g_{lum}$  at 526 nm ( $+0.10, -0.14$ ) and 400 nm ( $+0.22, -0.23$ ), respectively (Fig. 7f). These values were comparable to those of the reported supramolecular helixene polymers and other LC systems.<sup>72–75</sup> Furthermore, the CPL emission of phosphahelicenes was blue-shifted about 14–19 nm in LC films compared to their solid fluorescence. The blue-shifted emission was also confirmed in doped PMMA matrices (Fig. S47†), which assuredly revealed a uniform dilution and suppressed  $\pi$ – $\pi$  stacking of emitters in LCs. Nevertheless,  $6b-N^*$  exhibited an

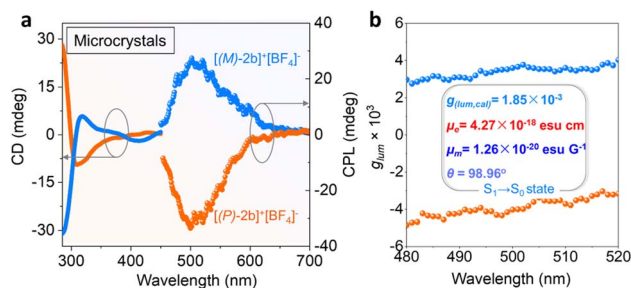


Fig. 6 (a) CD and CPL spectra of enantiomerically enriched  $[2b]^+[BF_4]^-$  microcrystals at room temperature ( $\lambda_{ex} = 360$  nm). (b) Corresponding experimental  $g_{lum}$  factors of the CPL spectra and TD-DFT simulative electron ( $\mu_e$ ), magnetic transition dipole moments ( $\mu_m$ ), and their angle ( $\theta_{e-m}$ ),  $g_{lum(cal)}$ .

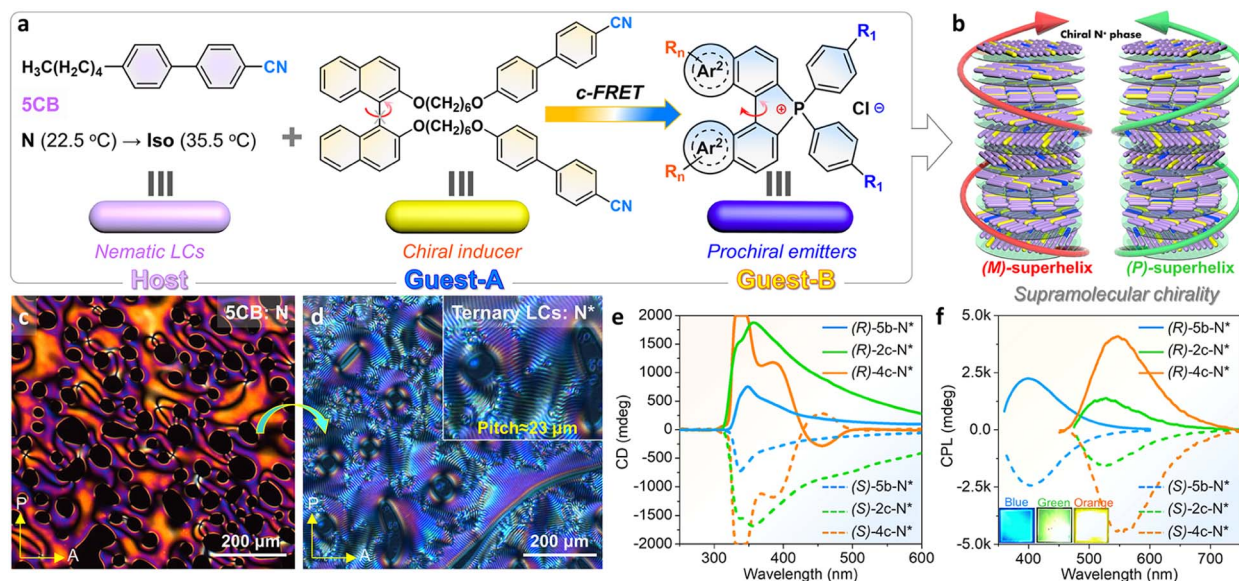


Fig. 7 (a) Schematic illustration of the ternary chiral LC system. (b) Suprachiral assembly model of the N\* mesophase. (c) POM texture of pure 5CB at 25 °C. (d) POM texture of (S)-5b-N\* (1.5 wt% for (S)-guest-B and 2.0 wt% for [5c]<sup>+</sup>[Cl]<sup>−</sup>). (e) CD spectra of enantiomeric ternary chiral LC films (guest-A/4.0 wt% and (S)/(R)-guest-B/2.0 wt%) at 25 °C. (f) CPL spectra of enantiomeric ternary chiral LC films (guest-A/4.0 wt% and (S)/(R)-guest-B/2.0 wt%) at 25 °C ( $\lambda_{\text{ex}}$  = 350 nm).

integrated deep blue emission due to collective CPL contribution from the host and guests (Fig. S55a and S57a†). Interestingly, the CPL contribution of BINOL-CN has not been observed in 2c-N\* and 4c-N\* LCs. Although the emission of helicenes can be directly excited at 350 nm, the fluorescence output might be accompanied by partial FRET in this unique system. Both the 5CB host and BINOL-CN donor produced deep blue fluorescence at 382 nm which was predominated by the ICT transition between BINOL and cyanobiphenyls (Fig. S55†), which overlapped with the ICT absorption of the phosphahelicene acceptor (Fig. S56 and S57a†). Hence, we further explored the fluorescence of various molar proportions of [4c]<sup>+</sup>[Cl]<sup>−</sup> in host LCs. As molar ratios of helicenes gradually increased, the fluorescence intensity and decay of 5-CB@BINOL-CN appeared to decrease (Fig. S58†). These results provided further evidence for energy transfer from the donor to the acceptor.<sup>66,72</sup> In contrast, the guest [6b]<sup>+</sup>[Cl]<sup>−</sup> absorption onset peak (370 nm) was out of tune with the host emission region (382 nm), leading to an interrupted energy transfer between the donor and acceptor (Fig. 5a).

To reveal the mechanism of increased CPL emission in N\*-LCs, excitation wavelength-dependent CPL spectra of N\*-4c were also measured in quartzose cells (Fig. S59†). The CPL spectra of 4c-N\* displayed larger  $g_{\text{lum}}$  values in the excitation region of FRET ( $\lambda_{\text{em}}$  = 350 nm) than direct excitation at 400 nm, demonstrating that chiral FRET could successfully promote the enlargement effect of the induced CPL signal in an intrinsically helical assembly environment.<sup>62,76</sup> CPL emissions of emitters were interrelated to chiral BINOL-CN, indicating the formation of chirality transmission and coupling through the  $\pi$ - $\pi$ , dipole-dipole interactions of the polar aromatic units in the helical host-guest system.<sup>76</sup> In addition, no Bragg reflection and

structural color were observed in the visible light region due to the sizeable helical pitches, and chirality transmission was interrupted in the phase-separated devices (the N\*-LC layer and heliceneslayer were isolated, Fig. S59†), which firmly ruled out the physical reflection of CPL and verified the CPL transmission process.<sup>72,77</sup> This suggested that increased CPL of phosphahelicenes benefited from a spiral arrangement and chiral energy transmission.

## Conclusions

In summary, we have demonstrated the first case of Mn(III)-mediated C-P bond activation and intramolecular annulation of diphosphines by a radical phosphonium process, which gives access to highly emissive phosphahelicene cations and phosphoniums in satisfactory yields and with substrate universality and economic applicability. The electron-deficient structure and stereochemical information were revealed through experiments, calculations, and the anion exchange strategy. Further utilization of this skeleton was illustrated for constructing polychromatic fluorophores, CPL, and a supramolecular chiral LC mesophase, which displayed good tunability, high emission efficiency, and excellent CPL performance with ultrahigh  $g_{\text{lum}}$  values. Our findings provide an innovative synthesis protocol and insight for designing cationic phosphahelicenes *via* C-P bond activation toward desired bright emission, chiral amplification, and potential catalyst precursors.

## Data availability

Detailed experimental details and characterizations are listed in ESI† The data that support the findings of this study are available from the corresponding author on reasonable request.



## Author contributions

W. H. directed the project and revised the manuscript; B. Y. carried out synthesis and property studies, wrote, and revised the work. S. Y. performed the SC-XRD collections. The other authors provided assistance for optical measurements in the work. All authors have given approval to the final version of the manuscript.

## Conflicts of interest

The authors declare no conflict of interest.

## Acknowledgements

We gratefully thank the National Natural Science Foundation of China (No. 21871133) and the Natural Science Foundation of Jiangsu Province (No. BK20211146) and the Science, Technology, and Innovation Commission of Shenzhen Municipality (No. JCYJ20180307153251975) for financial support.

## Notes and references

- 1 A. Miyashita, A. Yasuda, H. Takaya, K. Toriumi, T. Ito, T. Souchi and R. Noyori, *J. Am. Chem. Soc.*, 1980, **102**, 7932–7934.
- 2 M. Berthod, G. Mignani, G. Woodward and M. Lemaire, *Chem. Rev.*, 2005, **105**, 1801–1836.
- 3 J.-P. Genet, T. Ayad and V. Ratovelomanana-Vidal, *Chem. Rev.*, 2014, **114**, 2824–2880.
- 4 W. Tang and X. Zhang, *Chem. Rev.*, 2003, **103**, 3029–3070.
- 5 Y. Wang, M. Liu, R. Cao, W. Zhang, M. Yin, X. Xiao, Q. Liu and N. Huang, *J. Med. Chem.*, 2013, **56**, 1455–1466.
- 6 W. Wang, Y. Ling, Y. Zhong, Z. Li, C. Tan and Z. Mao, *Angew. Chem.*, 2022, **134**, e202115247.
- 7 L.-Y. Yao, T. K.-M. Lee and V. W.-W. Yam, *J. Am. Chem. Soc.*, 2016, **138**, 7260–7263.
- 8 Y. J. Kong, Z. P. Yan, S. Li, H. F. Su, K. Li, Y. X. Zheng and S. Q. Zang, *Angew. Chem., Int. Ed.*, 2020, **59**, 5336–5340.
- 9 S. A. Macgregor, *Chem. Soc. Rev.*, 2007, **36**, 67–76.
- 10 L. Wang, H. Chen and Z. Duan, *Chem.-Asian J.*, 2018, **13**, 2164–2173.
- 11 Y. H. Lee and B. Morandi, *Coord. Chem. Rev.*, 2019, **386**, 96–118.
- 12 T. Jiang, H. Zhang, Y. Ding, S. Zou, R. Chang and H. Huang, *Chem. Soc. Rev.*, 2020, **49**, 1487–1516.
- 13 K. M. Crawford, T. R. Ramseyer, C. J. A. Daley and T. B. Clark, *Angew. Chem.*, 2014, **126**, 7719–7723.
- 14 X. Qiu, M. Wang, Y. Zhao and Z. Shi, *Angew. Chem., Int. Ed.*, 2017, **56**, 7233–7237.
- 15 M. Lei, X. Chen, Y. Wang, L. Zhang, H. Zhu and Z. Wang, *Org. Lett.*, 2022, **24**, 2868–2872.
- 16 Z. Lian, B. N. Bhawal, P. Yu and B. Morandi, *Science*, 2017, **356**, 1059–1063.
- 17 H. Kawai, W. J. Wolf, A. G. Dipasquale, M. S. Winston and F. D. Toste, *J. Am. Chem. Soc.*, 2016, **138**, 587–593.
- 18 K. Baba, M. Tobisu and N. Chatani, *Org. Lett.*, 2015, **17**, 70–73.
- 19 K. Baba, M. Tobisu and N. Chatani, *Angew. Chem., Int. Ed.*, 2013, **52**, 11892–11895.
- 20 S. Nieto, P. Metola, V. M. Lynch and E. V. Anslyn, *Organometallics*, 2008, **27**, 3608–3610.
- 21 X. Zhang, Y. Jiang, Q. Ma, S. Hu and S. Liao, *J. Am. Chem. Soc.*, 2021, **143**, 6357–6362.
- 22 A. Belyaev, Y.-T. Chen, Z.-Y. Liu, P. Hindenberg, C.-H. Wu, P.-T. Chou, C. Romero-Nieto and I. O. Koshevoy, *Chem.-Asian J.*, 2019, **25**, 6332–6341.
- 23 L. Pang, Q. Sun, Z. Huang, G. Li, J. Liu, J. Guo, C. Yao, J. Yu and Q. Li, *Angew. Chem., Int. Ed.*, 2022, **61**, e202211710.
- 24 M. Gicquel, Y. Zhang, P. Aillard, P. Retailleau, A. Voituriez and A. Marinetti, *Angew. Chem., Int. Ed.*, 2015, **54**, 5470–5473.
- 25 Y. Shen and C.-F. Chen, *Chem. Rev.*, 2012, **112**, 1463–1535.
- 26 K. Yavari, P. Aillard, Y. Zhang, F. Nuter, P. Retailleau, A. Voituriez and A. Marinetti, *Angew. Chem., Int. Ed.*, 2014, **53**, 861–865.
- 27 N. Saleh, C. Shen and J. Crassous, *Chem. Sci.*, 2014, **5**, 3680–3694.
- 28 K. Dhbaibi, L. Favereau and J. Crassous, *Chem. Rev.*, 2019, **119**, 8846–8953.
- 29 S. Nishigaki, K. Murayama, Y. Shibata and K. Tanaka, *Mater. Chem. Front.*, 2018, **2**, 585–590.
- 30 R. Mokrai, A. Mocanu, M. P. Duffy, T. Vives, E. Caytan, V. Dorcet, T. Roisnel, L. Nyulászi, Z. Benkő, P.-A. Bouit and M. Hissler, *Chem. Commun.*, 2021, **57**, 7256–7259.
- 31 K. Yavari, W. Delaunay, N. De Rycke, T. Reynaldo, P. Aillard, M. Srebro-Hooper, V. Y. Chang, G. Muller, D. Tondelier, B. Geffroy, A. Voituriez, A. Marinetti, M. Hissler and J. Crassous, *Chem.-Asian J.*, 2019, **25**, 5303–5310.
- 32 Y. Sawada, S. Furumi, A. Takai, M. Takeuchi, K. Noguchi and K. Tanaka, *J. Am. Chem. Soc.*, 2012, **134**, 4080–4083.
- 33 K. Nakano, H. Oyama, Y. Nishimura, S. Nakasako and K. Nozaki, *Angew. Chem.*, 2012, **124**, 719–723.
- 34 M. Widhalm, C. Aichinger and K. Mereiter, *Tetrahedron Lett.*, 2009, **50**, 2425–2429.
- 35 E. Rémond, J. Fehrentz, L. Liénart, S. Clement, J. Baneres and F. Cavelier, *Chem.-Eur. J.*, 2022, **28**, e202201526.
- 36 L. Frederic, A. Desmarchelier, L. Favereau and G. Pieters, *Adv. Funct. Mater.*, 2021, **31**, 2010281.
- 37 Y. Im, M. Kim, Y. J. Cho, J.-A. Seo, K. S. Yook and J. Y. Lee, *Chem. Mater.*, 2017, **29**, 1946–1963.
- 38 K. Kawara, G. Tsuji, Y. Taniguchi and S. Sasaki, *Chem.-Asian J.*, 2017, **23**, 1763–1769.
- 39 X. Xiao, Q. Cheng, S. T. Bao, Z. Jin, S. Sun, H. Jiang, M. L. Steigerwald and C. Nuckolls, *J. Am. Chem. Soc.*, 2022, **144**, 20214–20220.
- 40 M. Grzybowski, K. Skonieczny, H. Butenschön and D. T. Gryko, *Angew. Chem., Int. Ed.*, 2013, **52**, 9900–9930.
- 41 D. J. Ager, M. B. East, A. Eisenstadt and S. A. Laneman, *Chem. Commun.*, 1997, 2359–2360.
- 42 S. Gladiali, A. Dore, D. Fabbri, O. De Lucchi and G. Valle, *J. Org. Chem.*, 1994, **59**, 6363–6371.
- 43 A. kumar Swain, K. Kolanji, C. Stapper and P. Ravat, *Org. Lett.*, 2021, **23**, 1339–1343.





- 44 P. Ravat, R. Hinkelmann, D. Steinebrunner, A. Prescimone, I. Bodoky and M. Juriček, *Org. Lett.*, 2017, **19**, 3707–3710.
- 45 R. H. Janke, G. Haufe, E. U. Würthwein and J. H. Borkent, *J. Am. Chem. Soc.*, 1996, **118**, 6031–6035.
- 46 M. Oki, *Top. Stereochem.*, 1983, **14**, 1–81.
- 47 M. Toya, T. Omine, F. Ishiwari, A. Saeki, H. Ito and K. Itami, *J. Am. Chem. Soc.*, 2023, **145**, 11553–11565.
- 48 Y. Okamoto, N. Iwamoto, S. Toki and S. Takamuku, *Bull. Chem. Soc. Jpn.*, 1987, **60**, 277–282.
- 49 K. Wei, K. Luo, F. Liu, L. Wu and L.-Z. Wu, *Org. Lett.*, 2019, **21**, 1994–1998.
- 50 Chaolumen, M. Murata, A. Wakamiya and Y. Murata, *Angew. Chem., Int. Ed.*, 2017, **56**, 5082–5086.
- 51 M. Zhao, S. H. Pun, Q. Gong and Q. Miao, *Angew. Chem., Int. Ed.*, 2021, **60**, 24124–24130.
- 52 J. Liu, A. Narita, S. Osella, W. Zhang, D. Schollmeyer, D. Beljonne, X. Feng and K. Müllen, *J. Am. Chem. Soc.*, 2016, **138**, 2602–2608.
- 53 Y. Zou, Y. Han, S. Wu, X. Hou, C. H. E. Chow and J. Wu, *Angew. Chem., Int. Ed.*, 2021, **60**, 17654–17663.
- 54 N. Sharma, H.-B. Zou, Y.-M. Lee, S. Fukuzumi and W. Nam, *J. Am. Chem. Soc.*, 2021, **143**, 1521–1528.
- 55 L. Liu, L. Li, X. Wang, R. Sun, M. D. Zhou and H. Wang, *Org. Lett.*, 2021, **23**, 5826–5830.
- 56 E. R. Johnson, S. Keinan, P. Mori-Sánchez, J. Contreras-García, A. J. Cohen and W. Yang, *J. Am. Chem. Soc.*, 2010, **132**, 6498–6506.
- 57 L.-J. Xu, C.-Z. Sun, H. Xiao, Y. Wu and Z.-N. Chen, *Adv. Mater.*, 2017, **29**, 1605739.
- 58 P. Tao, S. J. Liu and W. Y. Wong, *Adv. Opt. Mater.*, 2020, **8**, 1–21.
- 59 T. Buhse, J.-M. Cruz, M. E. Noble-Terán, D. Hochberg, J. M. Ribó, J. Crusats and J.-C. Micheau, *Chem. Rev.*, 2021, **121**, 2147–2229.
- 60 F. Wang, F. Gan, C. Shen and H. Qiu, *J. Am. Chem. Soc.*, 2020, **142**, 16167–16172.
- 61 A. I. Boldyrev and L.-S. Wang, *Chem. Rev.*, 2005, **105**, 3716–3757.
- 62 H. Fallah-Bagher-Shaidei, C. S. Wannere, C. Corminboeuf, R. Puchta and P. v. R. Schleyer, *Org. Lett.*, 2006, **8**, 863–866.
- 63 E. Cherni, B. Champagne, S. Ayadi and V. Liégeois, *Phys. Chem. Chem. Phys.*, 2019, **21**, 14678–14691.
- 64 G. Naulet, L. Sturm, A. Robert, P. Dechambenoit, F. Röhricht, R. Herges, H. Bock and F. Durola, *Chem. Sci.*, 2018, **9**, 8930–8936.
- 65 T. Luo, Y. Wang, J. Hao, P. A. Chen, Y. Hu, B. Chen, J. Zhang, K. Yang and Z. Zeng, *Angew. Chem., Int. Ed.*, 2023, **62**, e202214653.
- 66 K. Usui, N. Narita, R. Eto, S. Suzuki, A. Yokoo, K. Yamamoto, K. Igawa, N. Iizuka, Y. Mimura, T. Umeno, S. Matsumoto, M. Hasegawa, K. Tomooka, Y. Imai and S. Karasawa, *Chem.-Asian J.*, 2022, **28**, e202202922.
- 67 X. Cao, D. Zhang, S. Zhang, Y. Tao and W. Huang, *J. Mater. Chem. C*, 2017, **5**, 7699–7714.
- 68 J. Luo, Z. Xie, J. W. Y. Lam, L. Cheng, H. Chen, C. Qiu, H. S. Kwok, X. Zhan, Y. Liu, D. Zhu and B. Z. Tang, *Chem. Commun.*, 2001, 1740–1741.
- 69 T. Mori, *Chem. Rev.*, 2021, **121**, 2373–2412.
- 70 P. Xing and Y. Zhao, *Acc. Chem. Res.*, 2018, **51**, 2324–2334.
- 71 M. Liu, L. Zhang and T. Wang, *Chem. Rev.*, 2015, **115**, 7304–7397.
- 72 Y. Wu, C. Yan, X.-S. Li, L. H. You, Z.-Q. Yu, X. Wu, Z. Zheng, G. Liu, Z. Guo, H. Tian and W.-H. Zhu, *Angew. Chem., Int. Ed.*, 2021, **60**, 24549–24557.
- 73 B. A. San Jose, S. Matsushita and K. Akagi, *J. Am. Chem. Soc.*, 2012, **134**, 19795–19807.
- 74 X. Yang, X. Jin, T. Zhao and P. Duan, *Mater. Chem. Front.*, 2021, **5**, 4821–4832.
- 75 J. Wade, J. R. Brandt, D. Reger, F. Zinna, K. Y. Amsharov, N. Jux, D. L. Andrews and M. J. Fuchter, *Angew. Chem.*, 2021, **133**, 224–229.
- 76 K. Yao, Y. Shen, Y. Li, X. Li, Y. Quan and Y. Cheng, *J. Phys. Chem. Lett.*, 2021, **12**, 598–603.
- 77 J. Yan, F. Ota, B. A. San Jose and K. Akagi, *Adv. Funct. Mater.*, 2017, **27**, 1604529.

